Time-Resolved Heat Transfer Measurements on the Tip Wall of a Ribbed Channel Using a Novel Heat Flux Sensor—Part II: Heat Transfer Results

Sean Jenkins
e-mail: sean.jenkins@itlr.uni-stuttgart.de

Jens von Wolfersdorf

Bernhard Weigand

Institute of Aerospace Thermodynamics,
University of Stuttgart,
Pfaffenwaldring 31,
70569 Stuttgart, Germany

Tim Roediger

Helmut Knauss

Ewald Kraemer

Institute of Aerodynamics and Gas Dynamics,
University of Stuttgart,
Pfaffenwaldring 21,
70569 Stuttgart, Germany

Measurements using a novel heat flux sensor were performed in an internal ribbed channel representing the internal cooling passages of a gas turbine blade. These measurements allowed for the characterization of heat transfer turbulence levels and unsteadiness not previously available for internal cooling channels. In the study of heat transfer, often the fluctuations can be equally as important as the mean values for understanding the heat loads in a system. In this study, comparisons are made between the time-averaged values obtained using this sensor and detailed surface measurements using the transient thermal liquid crystal technique. The time-averaged heat flux sensor and transient TLC results showed very good agreement, validating both methods. Time-resolved measurements were also corroborated with hot film measurements at the wall at the location of the sensor to better clarify the influence of unsteadiness in the velocity field at the wall on fluctuations in the heat flux. These measurements resulted in turbulence intensities of the velocity and heat flux of 20%. The velocity and heat flux integral length scales were about 60% and 35% of the channel width, respectively, resulting in a turbulent Prandtl number of 1.7 at the wall. [DOI: 10.1115/1.2472417]

Keywords: internal cooling, ribs, turbulence, heat transfer

Introduction

Engine designers are continuously striving to increase the heat transfer levels in internal passages of turbine blades. This results in higher levels of cooling and thus permits higher turbine inlet temperatures, which lead to higher overall engine efficiency. It is clear that a greater understanding of the heat transfer processes in internal passages will assist in creating better designs.

It is with this goal in mind that experiments were undertaken to measure time-resolved heat fluxes at positions in an internally ribbed channel. To fully understand the heat loads in a system such as this, fluctuations in the heat flux can be equally or more important than the time-mean values. Identification of the range of frequencies present in the turbulence field and which of those frequencies are responsible for increasing heat transfer can also be helpful in improvement or validation of computational codes.

Many research groups have investigated heat transfer in internal passages; however, heat transfer turbulence spectra in gas turbine applications have been mainly investigated for external flows. A recent study by Nix and Diller [1] investigated the physical mechanism for heat transfer on a cylinder stagnation point by making simultaneous measurements of the velocity field and heat flux at the surface. They found a strong coherence between the signals at lower frequencies, indicating that the penetration of large-scale eddies through the boundary layer were responsible for augmentation of the heat transfer. They used a heat flux microsensor for the heat flux measurements, which was capable of resolv-

ing the range of frequencies in the low speed tunnel. They argued that the cylinder stagnation point is a good representation of the leading edge of a vane or blade, thus allowing the study of external blade heat transfer on a simplified model. Both velocity and heat flux spectra were reported, as well as turbulence intensities of both velocity and heat flux. An analytical model developed in a previous paper by Nix et al. [2], based on the turbulence length scale and turbulence intensity, showed good agreement with the augmentation of the heat flux by freestream turbulence.

In previous work by Holmberg and Diller [3] using the same sensor, measurements of external heat transfer were made at three positions on the pressure surface of a turbine blade. They investigated the effects of grid-generated turbulence conditions on the heat transfer and found that the mean heat transfer was higher for a smaller length scale given constant turbulence intensity.

Moss and Oldfield [4] made time-resolved measurements using thin-film gages and hot wires in a flat-plate boundary layer with high levels of freestream turbulence. They made simultaneous measurements of the velocity and heat flux and showed that turbulent eddies from the freestream penetrated the boundary layer, enhancing the heat transfer.

With respect to time mean results, data are very sparse for the tip wall of a two-pass high aspect ratio channel. A companion study [5] shows limited results on the tip wall for the same channel at one Reynolds number; however, the focus of that study is on heat transfer in the outlet channel. Hirota et al. [6] showed results on the tip wall for a low aspect ratio (1:2) channel using the sublimation method. They observed a high heat transfer area due to impingement of the flow in the turning region. However, the channel did not include ribs; thus, effects of rib-induced secondary flows were not investigated. Schnieder et al. [7] showed heat transfer distributions on the tip wall of a short rectangular (1:2) channel with 45 deg ribs and several flow-guide vane configurations in the bend region.
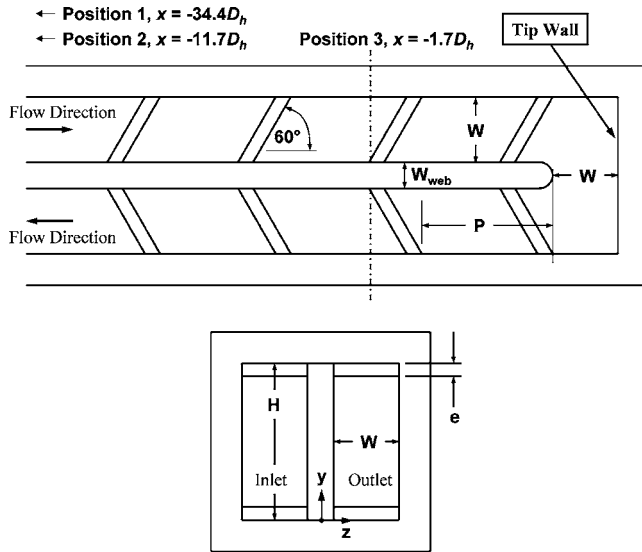
Fig. 1 Schematic top view and cross section of the test channel with 60 deg ribs
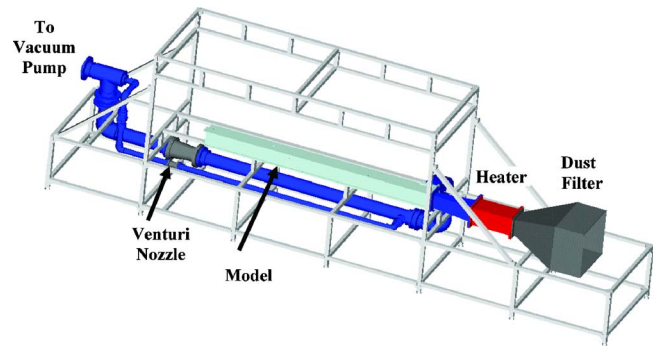

Fig. 2 Diagram of test rig

Although the secondary flows generated by angled ribs have been fairly well studied [8–10], the effects of these secondary flows on the tip-wall heat transfer have not. This critical region has been investigated in detail in the present study, both with respect to mean heat transfer distributions and time-resolved results.

The current study seeks to fill a gap in the literature by documenting the distribution of mean heat transfer on the tip wall of a high aspect ratio channel with angled ribs. Furthermore, it seeks to demonstrate the capability of a novel heat flux sensor to provide both mean and time-resolved heat flux information in such a channel. Measurements in this critical region of an internal passage should assist in the validation of computational codes, and shed light on the nature of the turbulence present at the tip wall.

Facility and Instrumentation

Measurements were made on the tip wall of a 4:1 aspect ratio, two-pass channel. The channel, shown in Fig. 1, was 2.4 m long and each pass had a width of $W=42$ mm and height of $H=168$ mm, resulting in a hydraulic diameter of $D_h=1.6W=67.2$ mm. The inlet channel had an entrance length of $L_e=1.524$ m to ensure hydrodynamically and thermally fully developed conditions preceding the measurement section with a length of $L_m=0.840$ m. This entrance length was required to accommodate a minimum of 15 ribs, which has been shown in several previous studies to provide fully developed heat transfer result in ribbed channels [11–13]. The inlet and outlet channels were connected by a sharp 180 deg bend. The divider wall had a thickness of $W_{web}=0.4W$ and the tip of the divider wall was radiused as shown in Fig. 1. The ribs had a square cross section and a height of $e/H=0.05$ (or $e/D_h=0.125$) and a spacing of $P/e=10$. They were arranged in a parallel fashion at an angle of $\alpha=60$ deg to the flow direction.

Transient Liquid Crystal Technique. The transient liquid-crystal technique (TLC) was used to determine the heat transfer coefficient distribution on the tip wall. The channel was constructed from 20 mm thick Plexiglas to offer good optical access and to fulfill the semi-infinite wall assumption required with this method. Inner surfaces of the channel were first coated with narrow band liquid crystals (Hallcrest BM/R31C1W/C17-10) and then black paint to provide high intensity in the colorplay of the liquid crystals. A CCD camera (Sony RBG Video Camera Module, Model XC-711P) was positioned to capture the color change

of the liquid crystal on the tip wall during the transient experiment, and this was recorded on digital video tape using a Sony digital video cassette recorder (Model GV-D900E PAL). The digital video was transferred to computer from the recorder for data analysis via FIREWIRE.

The temperature step for the transient liquid-crystal technique was provided by a mesh heater, which was square in cross section and was based on the design of Wang et al. [14] and Ireland et al. [15]. Airflow entered the test rig through a dust filter, as shown in Fig. 2, and after passing through the heater section, flowed through a contraction section, which reduced to the dimensions of the entrance of the inlet channel. The outlet of the channel was connected by a series of pipes to a vacuum pump system capable of flow rates up to 2.5 kg/s. As shown in Fig. 2, the piping system included a Venturi nozzle for measurements of the mass flow rate and also contained a valve for flow regulation.

In order to evaluate the experimental results, solution of the one-dimensional (1D) conduction equation with the assumption of a semi-infinite wall and convective boundary condition is required. The nondimensional temperature at the surface $(x=0)$ is given by

$$\frac{T_W - T_0}{T_B - T_0} = 1 - \exp\left(\frac{h^2 \alpha_w t}{k_w^2}\right) \text{erfc}\left(\frac{h\sqrt{\alpha_w t}}{k_w}\right) \qquad (1)$$

with initial and boundary conditions of

$$t = 0: \ T = T_0$$

$$x = 0: \ -k\frac{\partial T}{\partial x} = h(T_W - T_B)$$

$$x \rightarrow \infty: \ T = T_0 \qquad (2)$$

where T_0 is the initial fluid temperature, T_B is the bulk temperature, h is the heat transfer coefficient, and α_w and k_w are the thermal diffusivity and conductivity of the wall material, respectively. Since the bulk temperature at the measurement position was also a function of time, the time history of the temperature step must be incorporated into the solution of Eq. (1) with the help of Duhamel's superposition theorem [16]. This results in the following expression:

$$T_W - T_0 = \sum_{i=1}^{N} (T_{B,i} - T_{B,i-1}) \left[1 - \exp\left(\frac{h^2 \alpha_w(t - t_i)}{k_w^2}\right) \right.$$
$$\left. \times \text{erfc}\left(\frac{h\sqrt{\alpha_w(t - t_i)}}{k_w}\right) \right] \qquad (3)$$

A transient heat transfer test was begun once constant flow rate and initial temperature conditions were obtained. Then power from a DC supply to the heater was switched on impulsively to provide the temperature step and the color change of the liquid crystals was recorded as the hot mainstream was imposed on the
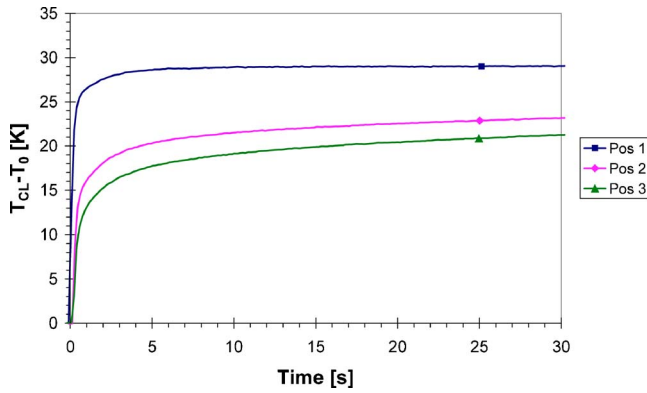
Fig. 3 Centerline temperature profiles for positions upstream of the bend

Fig. 4 Schematic cross section of the ALTP heat flux sensor module

cool surfaces. The thermal liquid-crystal color change was analyzed to determine the time point at which each pixel reached the calibrated green hue value (hue between 105 and 115 on 0–255 scale). Using the time of thermal liquid-crystal indication and a local time-resolved bulk temperature profile, Eq. (3) was solved for the heat transfer coefficient.

Measurements of the centerline temperature were made using Agilent 24307 data acquisition units with thermocouples placed at $34.4D_h$, $11.7D_h$, and $1.7D_h$ upstream of the bend in the inlet channel. This temperature data was used to account for the variation in bulk temperature both with position and time. As shown in Fig. 3, due to heat flux from the fluid to the wall, the time-dependent temperature history changed with position in the channel. Close to the heater, the profile was nearly a step change; however, further downstream the initial step was smoothed and the temperature was lower at each downstream position. To accurately calculate the local heat transfer coefficient, the local bulk temperature profile was calculated at the entrance to the bend using a model developed by von Wolfersdorf et al. [17] based on a mean heat balance along the inlet channel. The interpolation procedure is based on a 1D heat balance calculating the temperature drop over an infinitesimal short section using the heat flux into the walls assuming a mean heat transfer over the perimeter. This model was expanded with help from the Duhamel principle to account for a time-varying temperature profile as the starting point for the calculation. Thus, the bulk temperature history $[T_B(x,t)]$ was calculated for each axial position in the channel with the following:

$$\frac{T_B(x,t) - T_0}{T_E(t) - T_0} = 1 - \left[1 - \exp\left(\frac{-\bar{h}\mathcal{P}}{\dot{m}c_p} x\right) \right]$$
$$\times \exp\left(\frac{\bar{h}^2 \alpha_w t}{k_w^2} A^2\right) \mathrm{erfc}\left(\bar{h} A \sqrt{\frac{t\alpha_w}{k_w^2}}\right) \quad (4)$$

$$\text{with} \quad A = \frac{1 - \exp\left(\frac{-\bar{h}\mathcal{P}}{\dot{m}c_p} x\right)}{\frac{\bar{h}\mathcal{P}}{\dot{m}c_p} x} \quad (5)$$

$$\bar{h}(x) = \frac{\int_{x'=0}^{x} h T_B \, dx'}{\int_{x'=0}^{x} T_B \, dx'} \quad (6)$$

where $\bar{h}$ is the average heat transfer coefficient, $\mathcal{P}$ is the perimeter of the cross section, $\dot{m}$ is the mass flow rate, c_p is the specific heat
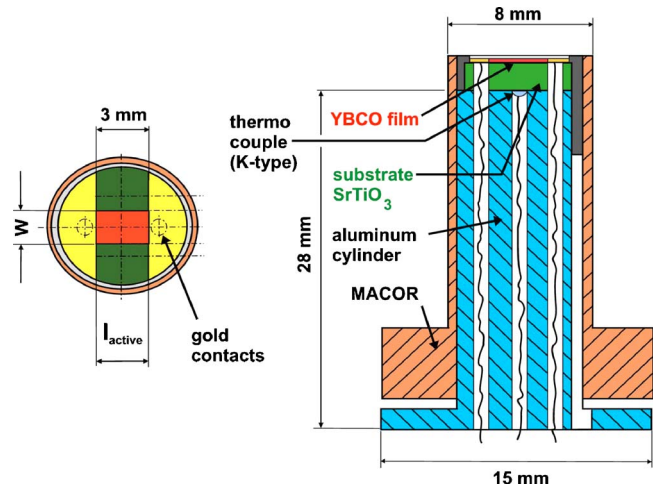
of the fluid at constant pressure, α_w and k_w are the thermal diffusivity and conductivity of the wall material, respectively, and $T_E(t)$ is the temperature history at the initial position in the calculation. This allowed for the calculation of the temperature history at the entrance to the bend region, which was used for the evaluation of the heat transfer for the inlet side of the tip wall. A second temperature history was computed at the midpoint of the bend at the beginning of the outlet for evaluation of results on the outlet side of the tip wall.

Measurements described fully in [5] showed that the centerline temperature agreed well with the mean temperature history. Using a numerical calculation of the velocity field from a preliminary study, comparisons between the mean temperature and a calculated bulk temperature were made and differences were found to be negligible. Therefore, the centerline temperature history was used in place of the bulk temperature history for all calculations of heat transfer coefficients.

Atomic Layer Thermopile (ALTP) Heat Flux Sensor. Time-resolved heat flux measurements were acquired using an atomic layer thermopile (ALTP) heat flux sensor, which was originally developed as a detector for optical radiation. It uses the thermopile effect created by a temperature gradient over a yttrium-barium-copper-oxide ($YBa_2Cu_3O_{3-d}$) crystal (later referred to as YBCO). Copper oxide layers and YBCO interlayers form atomic thermocouples connected in series. The thermopile works on the principle of the transverse Seebeck effect, caused by the anisotropy of the YBCO film in combination with a tilt angle of the crystal with respect to the film surface normal. A temperature gradient over the film creates a thermoelectric field E

$$\vec{E} = \vec{S} \nabla \vec{T} \quad (7)$$

where $\vec{S}$ is the Seebeck tensor and $\nabla \vec{T}$ is the temperature gradient over the film.

It was shown that the signal of the ALTP is purely of thermoelectric origin, and laser calibration experiments showed a linear characteristic of the sensor over more than 11 orders of magnitude. Temperature gradients created by heat flux rates of a few milliwatts per square centimeter up to $20\ \mathrm{kW/cm^2}$ (damage threshold for a 1 ms pulse) are detectable. It responds to radiation over a very large wavelength range from infrared to ultraviolet. For a detailed discussion of the characteristics of the sensor, the reader is referred to Part 1 [18].

A schematic of the ALTP heat flux sensor is shown in Fig. 4, detailing the construction and arrangement of components. The active area of the sensors used in these experiments was

3×3 mm. The housing of the module was made of a ceramic insulator (MACOR) to achieve mainly one dimensional heat flux through the substrate and the cylinder.

The sensor was attached to an amplifier and then to a low-pass filter. For data acquisition, a Dewetron transient recorder with an Insight A/D board (14 bit, 800 kHz) was used. All measurements were taken using a 10 kHz low-pass filter and amplified by 8500.

Hot-Film Gage-Dantec Flush Mounting Probe (FMP). For comparison to the heat flux fluctuations, a hot film gage (DAN-TEC Flush Mounting Probe 55R45) with an active length of 0.4 mm operated by a DANTEC 56C20 temperature plug-in unit in a DANTEC 56C01 CTA system was used to measure velocity fluctuations. Fluctuations in the hot film gage signal, were correlated with the velocity fluctuations u'.

Computation of Turbulence Quantities. Fluctuations in the velocity and heat flux were calculated from the integration of the power spectral density as follows:

$$u'^2 = \int_0^\infty E_u(f)df \quad q'^2 = \int_0^\infty E_q(f)df \qquad (8)$$

With these quantities, the turbulence intensity and turbulent heat flux intensity were computed using the rms values divided by the mean

$$\mathrm{Tu} = \frac{\sqrt{u'^2}}{\bar{u}}, \quad \mathrm{Tu}_q = \frac{\sqrt{q'^2}}{\bar{q}} \qquad (9)$$

The integral time scale was computed from an integration of the autocorrelation function from the time signal of the velocity or heat flux where the autocorrelation function was computed from the normalized data,

$$R_{xx} = \int_0^\infty \hat{q}(t)\hat{q}(t+\tau)dt, \quad \text{where} \quad \hat{q}(t) = \frac{q-\bar{q}}{q'} \qquad (10)$$

and where $\bar{q}$ is the mean of the heat flux time signal and τ is the measurement interval. The autocorrelation function was integrated to determine the integral time scale as follows:

$$\mathrm{T}_f = \int_0^{\tau|R_{xx}=0} R_{xx}(\tau)d\tau \qquad (11)$$

An integral length scale, Λ_f, can be derived from this quantity by the use of a representative bulk velocity as follows:

$$\Lambda_f = U_{\mathrm{bulk}}\mathrm{T}_f, \quad \Lambda_q = U_{\mathrm{bulk}}\mathrm{T}_q \qquad (12)$$

The Kolmogorov scale was determined based on a point in the power density spectrum where the slope is approximately $m = -5/3$. This allows for calculation of the dissipation, ε, and thereby the Kolmogorov length scale, i.e. in the equilibrium range [19]:

$$E_u(k) = 0.5\varepsilon^{2/3}k^{-5/3} \qquad (13)$$

and

$$\eta = \left(\frac{\nu^3}{\varepsilon}\right)^{1/4} \qquad (14)$$

Uncertainty Analysis. Uncertainties related to the heat transfer measurements were estimated and are shown in Table 1. Uncertainties in the heat transfer measurements were based on temperature, time, and material property uncertainties. Temperature uncertainties were mainly bias errors as a result of the thermocouple calibration curve used and thus were not compounded in the use of a temperature evolution in the evaluation of heat transfer coefficients. The precision uncertainty in the temperature measurements was ~0.1 K. Uncertainties for the quantities presented in Table 1 are based on the precision uncertainty of the thermocouple measurements over the temperature range used (for (T_B-T_0)) and

Table 1 Uncertainties in measurement quantities

Quantity	ρ	Re	D_h	t	T_B-T_0	T_W-T_0
Uncertainty (%)	0.8	2.0	0.8	1.9	0.7	1.8

include uncertainties in the thermal liquid-crystal calibration (for (T_W-T_0)). Uncertainties in the material properties of the Plexiglas walls were estimated at 5%, resulting in a total uncertainty in the Nusselt number of ~8%.

Uncertainties for the ALTP heat flux sensor were estimated based on the uncertainty of the reference detector used in the calibration of the sensor (2%), the uncertainty in the absorption rate of the ALTP (5%), and the uncertainty due to the signal-to-noise ratio (5%), to give an overall error of 7.5%.

Results and Discussion

Measurements of the heat transfer were made on the tip wall of a two-pass ribbed duct by the transient thermal liquid-crystal technique and with the atomic layer thermopile (ALTP) heat flux sensor for a range of Reynolds numbers. Comparisons are made between the mean value of the point-specific time-resolved heat flux measurements and a symmetric point within the spatially resolved mean Nusselt number distributions. Time-resolved results were available from the ALTP heat flux sensor, allowing for computation of spectral distributions of heat flux and other turbulence statistics. Measurements using the ALTP heat flux sensor were made in two locations, one on the inflow side at a position of high heat flux, and one position on the outflow side where the heat flux was lower. This allowed for a comparison of how turbulence spectra and statistics differed on the tip wall. In addition, a hot-film gage, operated in CTA mode, provided measurements of the turbulent velocity spectra at the same location as the heat flux sensor.

Time-Mean Results. The distribution of the heat transfer coefficient, shown in Fig. 5, is representative of the typical pattern for the tip wall in this high aspect ratio ribbed channel. The orientation of the figure is downstream towards the tip wall (see Fig. 1). Symmetric peaks in the heat transfer coefficient on the left side of the figure are due to the rib induced secondary flows. The ribs induce a flow along the ribbed walls from the divider wall to the outer wall, which then recirculates back to the divider wall at the midplane, giving two symmetric secondary flow structures, shown in the schematic in Fig. 5. The location of the heat flux sensor is shown with a white cross in the lower left corner, centered at roughly $y/W=0.7$ and $z/W=-0.5$ and is referred to as Site 1. The sensor was placed in this position to take advantage of the symmetry of the results, thus allowing for a direct comparison between the heat flux sensor and thermal liquid-crystal results within the same experiment. This symmetry is shown in the schematic using results from a separate experiment without the heat flux sensor installed. In this example, agreement between the two symmetric positions was within 1%. The sensor was also placed in this location with relatively high heat flux and low gradients to reduce uncertainties in the heat flux sensor measurements. For the results shown at a Reynolds number of Re=100,000, the maximum heat transfer occurred at about $y/W=3.5$, $z/W=-0.4$, with a value of about Nu=475. The heat transfer coefficient reached the lowest value of Nu=275 at a point at midspan on the exit flow side of the tip wall ($z/W>0$). The divider wall position is shown schematically on the figure with dashed lines to indicate the inlet and outlet sides. The peak heat transfer levels were driven by impingement of the secondary flow vortices, but these secondary flows were disrupted in the bend region, and on the outlet side of the tip wall, heat transfer levels were much lower.

A comparison between the ALTP heat flux sensor and the symmetric position in the TLC Nusselt number distribution showed good agreement with values of Nu=467 and Nu=469, respec-
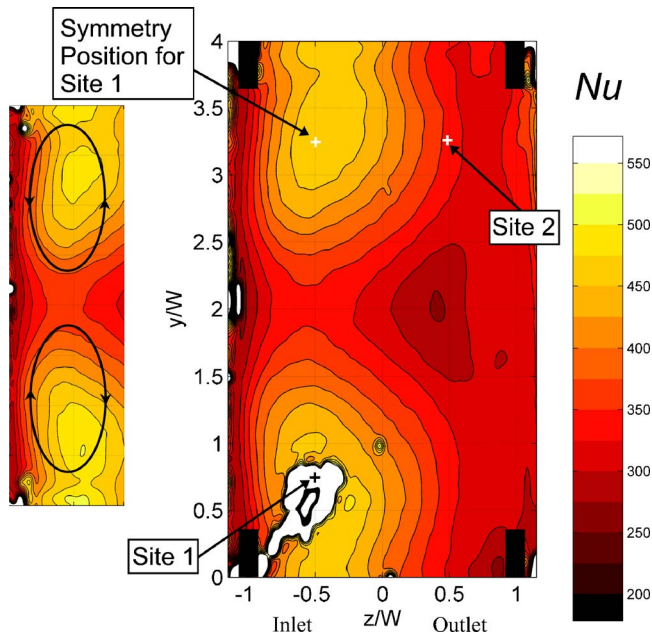
Fig. 5 Distribution of Nusselt number on the tip wall at Re =100,000 (with schematic of secondary flows)

tively, thus validating the procedure for determining the Nusselt number using the transient thermal liquid-crystal technique and also verifying the use of the ALTP heat flux sensor at these heat transfer levels and low Mach numbers. The heat flux was also measured for a second point positioned on the outflow side of the tip wall in the upper right corner (Site 2, in Fig. 5), where symmetry could also be used for comparisons. It should be noted that, due to the bulk fluid temperature rise during the test, the heat flux sensor recorded a slowly increasing heat flux, however, the heat transfer coefficient (or Nusselt number) was found to be constant.

Mean heat transfer coefficient distributions for a range of Reynolds numbers from Re=50,000 to 200,000 are shown in Fig. 6. In these figures, the scale is centered about a point determined by the average of the maximum and minimum Nusselt number. For all cases, the scale increment was $\Delta Nu=25$. It is immediately apparent from these figures that the pattern of the heat transfer was very similar in all cases, with symmetric islands of high heat transfer from the secondary flows on the inlet side and a lower level at midheight ($y/W=2.0$) on the outlet side. In contrast to these similarities, the gradient of the Nusselt number grew steadily with increasing Reynolds number, evident in the spacing of the contour levels. Less obvious was a shift in the position of the peak heat transfer, which moved downward with increasing Reynolds number, the most significant variation between Reynolds numbers of Re=50,000 and 100,000. The shape of the high heat transfer island also changed somewhat with Reynolds number. This was likely due to the higher momentum of the bulk flow at higher Reynolds numbers which constricted the secondary flow core.

In Fig. 7, a comparison for Site 1 between the heat transfer coefficients from the ALTP heat flux sensor and the symmetric point in the TLC distribution showed very good agreement. The data tracked very well over the entire Reynolds number range with a maximum difference of 6%.

Normally, the Nusselt number in a channel flow would be most appropriately normalized by the Dittus-Boelter equation [20]:

$$Nu_0 = 0.023\,Re^{4/5}\,Pr^{0.4} \tag{15}$$

However, as demonstrated in Fig. 8, this does not collapse the data. Instead, since the position of interest was on the tip wall, not on the channel wall, it experienced a flow condition much more

like a jet stagnation point flow. Lee et al. [21] found that for high Reynolds numbers, the Nusselt number at the stagnation point of a jet varied according to $Nu \propto Re^m$, where the exponent was cited as $m=0.565$. In the current study, data were found to collapse using

$$Nu = 0.69\,Re^{0.565} \tag{16}$$

In this case, the Reynolds number was based on the channel hydraulic diameter. This normalization flattened out the results, thus demonstrating the applicability of this relation for the given flow conditions.

A comparison of measurements from the ALTP heat flux sensor and the symmetric point in the transient liquid-crystal distributions also showed good agreement for Site 2 on the outlet portion of the tip wall. Figure 9 shows the Nusselt number for both measurement techniques at both Sites 1 and 2 in a log-log scale. The difference in slopes for the two sites can be seen in this figure, and a least-squares fit resulted in an exponent of about $m=0.7$ for Site 2, closer to the value for turbulent channel or boundary layer flow compared with Site 1.

Time-Resolved Results and Spectra. Time-resolved results were analyzed from the ALTP heat flux sensor for both Sites 1 and 2 to obtain spectra of the turbulent heat flux and to obtain turbulent heat flux intensities and turbulence length scales. Heat flux results were corroborated by measurements of the velocity in identical experiments using a flush mounted hot-film probe at Site 1, with data taken for several Reynolds numbers.

A time trace of the heat flux and velocity is shown in Fig. 10, where high-frequency fluctuations and the influence of large-scale structures can be seen in both traces. Since the data were taken during separate experiments, no direct correspondence may be inferred from the time signals; however, the period of large-scale (low-frequency) fluctuations appears to be similar for the two traces.

Spectra for the hot-film probe are shown in Fig. 11 for channel Reynolds numbers of Re=50,000, 100,000, and 150,000 at Site 1. The increase in energy is evident with increasing Reynolds number, as is the extension of the inertial subrange to higher frequencies. With increasing Reynolds number, the slope of the power spectral density approached the universal −5/3 law expected for isotropic turbulence in the non-viscous inertial subrange. Steeper slopes in the spectral results for lower Reynolds numbers suggest larger degrees of anisotropy and viscous effects in the turbulence field at Site 1. In general, as the Reynolds number increases, the boundary layer becomes thinner, and viscous effects less influential. Therefore, damping of fluctuations near the wall becomes less significant at higher Reynolds numbers and the expected universal power law is approached [22].

Turbulence intensity of the velocity fluctuations was calculated at about Tu=20% for all Reynolds numbers. Autocorrelation of the time-resolved results provided integral time scales on the order of 1 ms using Eqs. (10) and (11). Since the flow at the measurement location was similar to a jet stagnation point flow, the bulk channel velocity was used to calculate an integral length scale based on a representative velocity (Eq. (12)). This resulted in an integral length scale of about $\Lambda_f=25$ mm$=0.60W$ at a channel Reynolds number of Re=100,000. This indicates that the energy containing eddies were of a size a little larger than half the width of the channel. An estimate of the frequency of the Kolmogorov scale was made using Eqs. (13) and (14), resulting in a frequency of about 3×10^4 Hz for a channel Reynolds number of Re=100,000. This frequency was just to the right of the range of frequencies shown in Fig. 11.

Frequency domain results for the heat flux showed similar trends. As seen in Fig. 12, the slope of the power spectral density also decreased with increasing Reynolds number, approaching a value of about $m=-2.4$ at a Reynolds number of Re=200,000. Nix and Diller [1] measured turbulence spectra using a heat flux

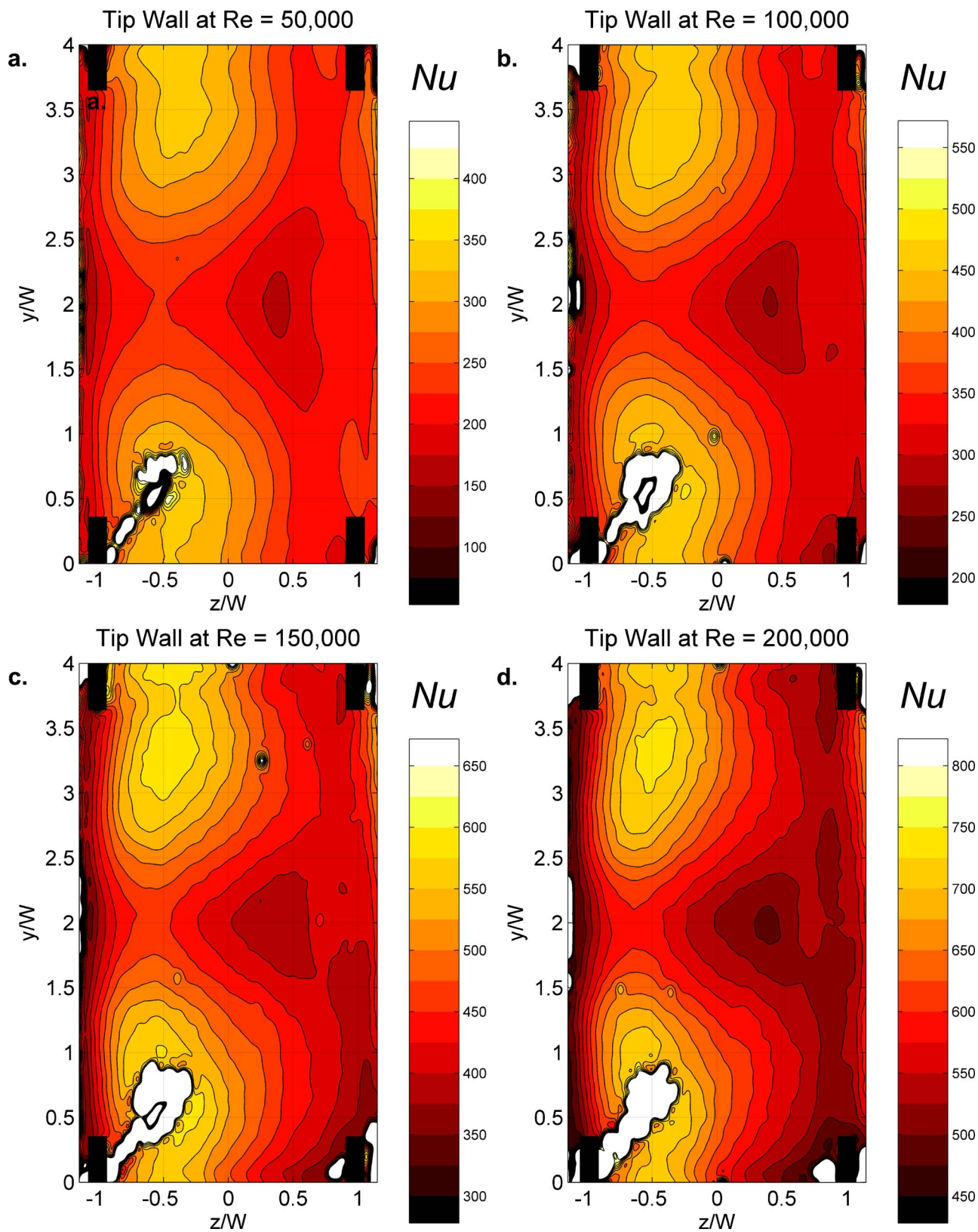**Fig. 6 Distribution of Nusselt number on the tip wall at Re=50,000 (*a*), 100,000, (*b*), 150,000 (*c*), and 200,000 (*d*)**

gage positioned at the stagnation point on a cylinder and reported results in terms of the power spectral density of the heat flux. Examination of their results revealed a slope of the heat flux power spectral density of about $m=-2.3$, which compares well to

the present work. Additionally, Lumley [23] suggested by dimensional analysis that the heat flux should follow a universal $-7/3$ law. The current results approach this suggested power law at the highest Reynolds numbers, thus reinforcing the evidence that a
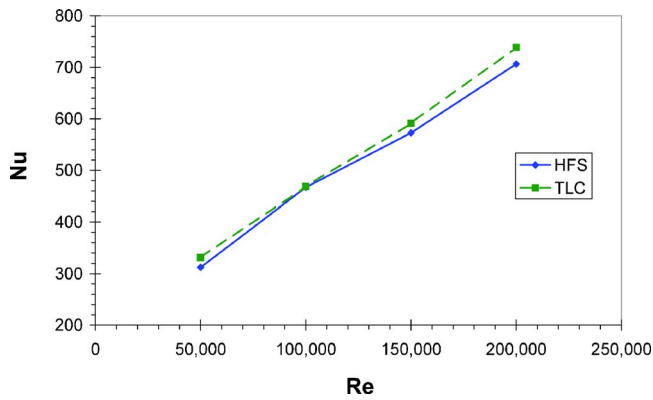
Fig. 7 Variation in the Nusselt number with Reynolds number for Site 1 of the heat flux sensor

Fig. 10 Heat flux and velocity time signals at Site 1 for Re = 100,000

power-law behavior is universal in the heat flux spectra as well. The heat flux spectra in the figure also show an increase in total energy in the flow with increasing Reynolds number and an increase in the extent of the inertial subrange.

The turbulent heat flux intensity Tu_q, which was found to be a little higher than $Tu_q = 20\%$ for all Reynolds numbers. This relatively high value for the turbulent heat flux intensity indicates that turbulence played a large role in the augmentation on the mean heat flux at this location on the wall. Integral time scales on the order of 1 ms were calculated from the time signal, similar to the velocity signal. However, the integral length scale from the heat flux for a channel Reynolds number of Re = 100,000 was calculated to be about $\Lambda_q = 15$ mm, or 35% of the channel width. This
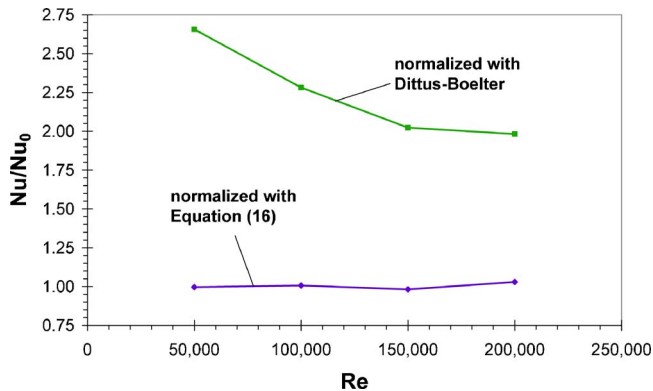

Fig. 8 Nusselt number for Site 1 normalized by the Dittus-Boelter equation and the relation given in Eq. (16)
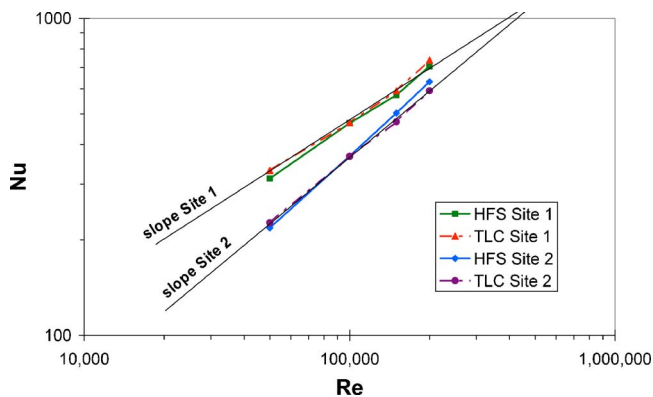

Fig. 11 Power spectral density of velocity versus frequency using a hot-film probe at Site 1

Fig. 9 Variation in the Nusselt number with Reynolds number for Sites 1 and 2 in log-log scale

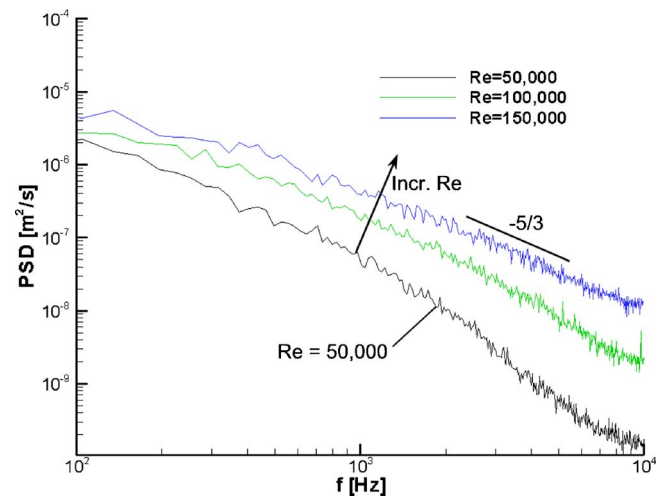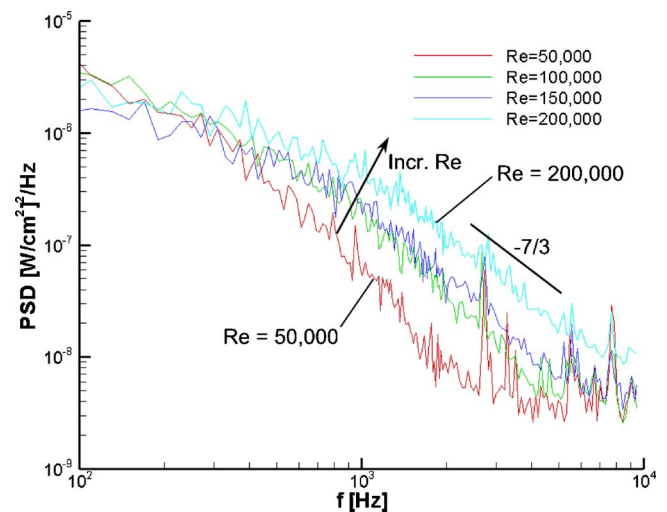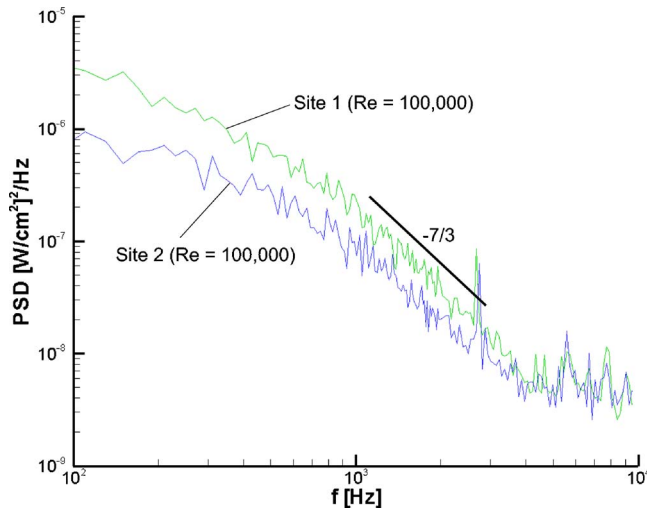**Fig. 12 Power spectral density of heat flux versus frequency using the ALTP heat flux sensor at Site 1**

Fig. 13 Power spectral density of heat flux versus frequency using the ALTP heat flux sensor comparing Sites 1 and 2 at Re=100,000

indicates that the most energetic eddies related to the heat flux were somewhat smaller than those in the turbulent velocity field. Although the heat flux sensor was influenced most strongly by fluctuations in the channel axial direction, i.e., directed at the tip wall, it appeared that the large scale eddies affecting the heat flux were bound by the channel width and the region of circulation of the secondary flows. Examination of the results in Nix and Diller [1] and Nix et al. [2] also showed a trend of this type between velocity and heat flux.

The ratio of the velocity integral length scale to the heat flux integral length scale, which may be interpreted as the turbulent Prandtl number [24]

$$\mathrm{Pr}_t = \frac{\Lambda_f}{\Lambda_q} \tag{17}$$

had a value at the wall of 1.67 at Site 1 for a channel Reynolds number of Re=100,000, which is in the range of values measured close to the wall for boundary layers and obtained from simple models shown in [25].

Behavior of the spectra at Site 2 was similar to that at Site 1, but the spectra contained less energy at all Reynolds numbers. A comparison between spectra measured at Sites 1 and 2 for a Reynolds number of Re=100,000 is shown in Fig. 13. The difference in energy at lower frequencies can be clearly seen, while the spectra both trail off at the same higher frequency. The data also show that, even at this lower Reynolds number, the spectra approached the −7/3 law.

The spectra followed the same trends with Reynolds number for Site 2 as those shown in Fig. 12 for Site 1, but with lower energy at each Reynolds number. As for Site 1, the integral length scale was relatively large with a value of about $\Lambda_q=15$ mm$=0.35W$ at a channel Reynolds number of Re=100,000. This would be expected since the flow was constrained in the same fashion approaching both positions. At Site 2, the turbulent heat flux intensity was found to be a little higher than $\mathrm{Tu}_q=20\%$ for all Reynolds numbers.

Conclusions

Measurements of the mean heat flux on the tip wall of a two pass high aspect ratio (4:1) channel with angled ribs were made using a transient liquid-crystal technique. Concurrent measurements of both the mean and time-resolved heat flux were made with a novel heat flux sensor at two key locations on the tip wall to provide validation of both measurement methods and to pro-

vide additional information about the turbulence characteristics of the heat flux at these locations. Turbulence spectra for the velocity and heat flux at the wall were compared for a range of Reynolds numbers representative of heavy duty turbines.

Measurements of the mean Nusselt number on the tip wall demonstrated that the distribution of the mean heat transfer due to secondary flows was consistent over a range of Reynolds numbers. Comparisons between results from a transient liquid-crystal technique and a novel heat flux sensor showed very good agreement for two positions on the tip wall. Analysis of the variation in heat transfer with the Reynolds number demonstrated differences in the behavior of the flow field responsible for the heat flux at these locations. At the position of peak heat transfer on the inflow side of the tip wall (Site 1), the variation in Nusselt number with Reynolds number followed a trend more like that for jet stagnation point flow. At Site 2 on the outflow side of the tip wall, the trend was more similar to that found in turbulent channel or boundary layer flow.

Analysis of the time signal from a flush mounted hot film probe at Site 1 on the tip wall showed that the velocity spectrum approached the universal −5/3 power-law behavior for higher Reynolds numbers. Similar results for the same position for the heat flux showed that the spectra had a −7/3 slope in the nonviscous inertial subrange, consistent with dimensional analysis. Turbulence intensities of the velocity and heat flux were both ∼20%. Length scales were determined using the time signals and results showed the velocity integral length scale was ∼60% of the channel width, while the heat flux integral length scale was ∼35% of the channel width, resulting in a ratio of integral length scales (turbulent Prandtl number) at the wall of $\Lambda_f/\Lambda_q=1.67$. These results show the importance of turbulence on the tip wall heat transfer in internal ribbed channels.

Nomenclature

c_p = specific heat (J/kg K)
D_h = hydraulic diameter, 67.2×10^{-3} m
e = rib height (m)
H = channel height, 0.168 m
h = heat transfer coefficient (W/m² K)
$\bar{h}$ = upstream averaged heat transfer parameter, (W/m² K)
k_w = thermal conductivity of the wall, (W/m K)
L_e = entrance length for the channel inlet, 1.524 m
L_m = measurement region in channel, 0.840 m
M = slope of power spectrum
$\dot{m}$ = mass flow rate (kg/s)
Nu = Nusselt number, (hD_h/k)
Nu_0 = Nusselt number from the Dittus-Boelter equation
P = pitch between ribs
$\mathcal{P}$ = channel perimeter, 0.420 m
Pr_t = turbulent Prandtl number
R_{xx} = autocorrelation function
Re = Reynolds number, $(U_{\mathrm{bulk}}D_h/\nu)$
T_0 = initial temperature (K)
T_B = bulk temperature (K)
T_{CL} = centerline temperature (K)
T_E = inlet temperature (K)
T_W = wall temperature (K)
t = time (s)

Tu = turbulence intensity, (u'/u_{mean})

Tu_q = turbulent heat flux intensity, (q'/q_{mean})

U_{bulk} = bulk channel velocity (m/s)

W = channel width, 0.042 m

x = axial channel coordinate

y = coordinate across channel width

z = coordinate across channel height

α_w = thermal diffusivity of the wall (m²/s)

ε = dissipation (m²/s³)

Λ_f = turbulence integral length scale (m)

Λ_q = turbulence integral heat flux length scale (m)

ν = kinematic viscosity (m²/s)

τ = measurement interval (s)

T_f = turbulence integral time scale (s)

T_q = turbulence integral time scale from heat flux (s)

ρ = density (kg/m³)

References

[1] Nix, A. C., and Diller, T. E., 2005, "Experiments on the Physical Mechanism of Heat Transfer Augmentation by Freestream Turbulence at a Cylinder Stagnation Point," International Gas Turbine and Aeroengine Congress and Exposition, Reno-Tahoe, ASME Paper No. GT2005–68616.

[2] Nix, A. C., Diller, T. E., and Ng, W. F., 2004, "Experimental Measurements and Modeling of the Effects of Large-Scale Freestream Turbulence on Heat Transfer," International Gas Turbine and Aeroengine Congress and Exposition, Vienna, ASME Paper No. GT2004–53260.

[3] Holmberg, D. G., and Diller, T. E., 2005, "Simultaneous Heat Flux and Velocity Measurements in Transonic Turbine Cascade," ASME J. Turbomach., **127**, pp. 502–506.

[4] Moss, R. W., and Oldfield, M. L. G., 1996, "Effect of Free-Stream Turbulence on Flat-Plate Heat Flux Signals: Spectra and Eddy Transport Velocities," ASME J. Turbomach., **118**, pp. 461–467.

[5] Pape, D., Jenkins, S., von Wolfersdorf, J., Weigand, B., and Schnieder, M., 2006, "The Influence of Including a Partially Smooth Section in the 2nd Leg of an Internally Ribbed Two Pass Cooling Channel," International Gas Turbine and Aeroengine Congress and Exposition, Barcelona, ASME Paper No. GT2006–90802.

[6] Hirota, M., Fujita, H., Syuhada, A., Araki, S., Yoshida, T., and Tanaka, T., 1999, "Heat/Mass Transfer Characteristics in Two-Pass Smooth Channels With a Sharp 180-Deg Turn," Int. J. Heat Mass Transfer, **42**, pp. 3757–3770.

[7] Schnieder, M., Höcker, R., and von Wolfersdorf, J., 2001, "Heat Transfer and Pressure Loss in a 180 deg turn of a Rectangular, Rib-Roughened two Passage Channel," 5th World Conference on Experimental Heat Transfer, Fluid Mechanics and Thermodynamics, ExHFT5, Thessaloniki, Sep.

[8] Su, G., Chen, H. C., Han, J. C., and Heidmann, J. D., 2004, "Computation of Flow and Heat Transfer in Two-Pass Rotating Rectangular Channels (AR =1:1, AR=1:2, AR=1:4) with 45-Deg Angled Ribs by a Reynolds Stress Turbulence Model," International Gas Turbine and Aeroengine Congress and Exposition, Vienna, ASME Paper No. GT2004–53662.

[9] Abdel-Wahab, S., and Tafti, D. K., 2004, "Large Eddy Simulation of Flow and Heat Transfer in a Staggered 45° Ribbed Duct," International Gas Turbine and Aeroengine Congress and Exposition, Vienna, ASME Paper No. GT2004–53800.

[10] Viswanathan, A. K., and Tafti, D. K., 2005, "Detached Eddy Simulation of Flow and Heat Transfer in a Stationary Internal Cooling Duct With Skewed Ribs," International Gas Turbine and Aeroengine Congress and Exposition, Reno-Tahoe, ASME Paper No. GT2005–68118.

[11] Graham, A., Sewall, E., and Thole, K. A., 2004, "Flowfield Measurements in a Ribbed Channel Relevant to Internal Turbine Blade Cooling," International Gas Turbine and Aeroengine Congress and Exposition, Vienna, ASME Paper No. GT2004–53361.

[12] Han, J. C., and Park, J. S., 1988, "Developing Heat Transfer in Rectangular Channels With Rib Turbulators," Int. J. Heat Mass Transfer, **31**, pp. 183–195.

[13] Han, J. C., 1984, "Heat Transfer and Friction in Channels with Two Opposite Rib-Roughened Walls," ASME J. Heat Transfer, **106**, pp. 851–861.

[14] Wang, Z., Gillespie, D., and Ireland, P., 1996, "Advances in Heat Transfer Measurements Using Liquid Crystals," *Turbulent Heat Transfer (Engineering Foundation)*, San Diego, CA, pp. 1–25.

[15] Ireland, P., Neely, A., Gillespie, D., and Robertson, A., 1999, "Turbulent Heat Transfer Measurements Using Liquid Crystals," Int. J. Heat Fluid Flow **20**, pp. 355–367.

[16] Metzger, D. E., and Larson, D. E., 1986, "Use of Melting Point Surface Coatings for Local Convection Heat Transfer Measurements in Rectangular Channel Flows with 90-Deg Turns," ASME J. Heat Transfer, **108**, pp. 48–54.

[17] von Wolfersdorf, J., Hoecker, R., and Hirsch, C., 1998, "A Data Reduction Procedure for Transient Heat Transfer Measurements in Long Internal Cooling Channels," ASME J. Heat Transfer, **120**, pp. 314–321.

[18] Roediger, T., Knauss, H., Gaisbauer, U., Kraemer, E., Jenkins, S., and von Woldersdorf, J., 2008, "Time-Resolved Heat Transfer Measurements on the Tip Wall of a Ribbed Channel Using a Novel Heat Flux Sensor—Part I: Sensor and Benchmarks," ASME J. Turbomach., **130**, p. 011018.

[19] Pope, S. B., 2000, *Turbulent Flows*, Cambridge University Press, Cambridge, England.

[20] Incropera, F. P., and DeWitt, D. P., 1996, *Fundamentals of Heat and Mass Transfer*, 4th Ed., Wiley, New York.

[21] Lee, D., Greif, R., Lee, S. J., and Lee, J. H., 1995, "Heat Transfer From a Flat Plate to a Fully Developed Axisymmetric Impinging Jet," ASME J. Heat Transfer **117**, pp. 772–775.

[22] Bogard, D. G., and Thole, K. A., 1998, "Wall Bounded Turbulent Flows," *The Handbook of Fluid Dynamics*, CRC Press, Boca Raton, Sec. 13.5, pp. 13.50–13.63.

[23] Lumley, J. L., 1967, "Similarity and the Turbulent Energy Spectrum," Phys. Fluids, **10**(4), pp. 855–858.

[24] Schlichting, H., 1982, *Grenzschicht-Theorie*, Verlag G. Braun, Karlsruhe.

[25] Kays, W. M., Crawford, M. E., and Weigand, B., 2005, *Convective Heat and Mass Transfer*, 4th ed., McGraw-Hill, New York.